



Synthesis of magnetically recyclable spinel ferrite (MFe_2O_4 , $\text{M} = \text{Zn}$, Co , Mn) nanocrystals engineered by sol gel-hydrothermal technology: High catalytic performances for nitroarenes reduction



Islam Ibrahim^a, Ibraheem O. Ali^a, Tarek M. Salama^a, A.A. Bahgat^b,
Mohamed Mokhtar Mohamed^{c,*}

^a Al-Azhar University, Faculty of Science, Chemistry Department, Nasr City, Cairo, Egypt

^b Al-Azhar University, Faculty of Science, Physics Department, Nasr City, Cairo, Egypt

^c Benha University, Faculty of Science, Chemistry Department, Benha, Egypt

ARTICLE INFO

Article history:

Received 14 April 2015

Received in revised form 28 July 2015

Accepted 4 August 2015

Available online 10 August 2015

Keywords:

Nanoferrites

PVA template

MnFe_2O_4

Characterization

Nitroarenes reduction

ABSTRACT

Highly stable and magnetically recoverable MFe_2O_4 ($\text{M} = \text{Zn}$, Co , Mn) spinel ferrite nanoparticles; synthesized using sol gel-hydrothermal technology via utilizing polyvinyl alcohol surfactant, were proposed as heterogeneous catalysts for the reduction of nitroarenes. The morphological characteristics, structural exploration, surface, optical, vibrational and magnetic properties were performed using powder X-ray diffraction, high-resolution transmission electron microscopy, energy dispersive X-ray, N_2 sorptiometry, diffused UV–vis reflectance spectroscopy, FTIR, point of zero charge, vibrating sample magnetometer (VSM) and thermokinetic analysis via TGA technique. The results showed that MnFe_2O_4 exhibited the best performance in the reduction of 4-nitrophenol (4-NP), 2,4,6 tri-nitrophenol (2,4,6-NP) and 4-nitroaniline (4-NA) and revealed 100% conversion into the corresponding amino derivatives in 270 sec with rate constant equal 0.01061 s^{-1} , 0.01134 s^{-1} and 0.01355 s^{-1} , respectively. The superiority of the catalytic reduction of MnFe_2O_4 was due to increasing the pore radius and pore volume (6.75 nm , $0.227 \text{ cm}^3/\text{g}$) values compared to other nanoferrites. The synthesized nanoferrites indicate independence of the activity on crystallite sizes due to the insignificant margin of change (from 6 to 10 nm). Conversely, decreasing the activity of ZnFe_2O_4 was due to increasing the Zn^{2+} ions size that induces an increase in lattice parameter values and thus increases the long-range electron transfer between Fe^{2+} – Fe^{3+} ions. The MnFe_2O_4 catalyst that presented the highest saturation magnetization (135 emu/g) indicated the highest reduction potential for 4-NA comparatively in the presence of NaBH_4 and the reduction reaction followed pseudo first-order kinetics. Increasing the reduction performance of 4-NA compared to other nitroaromatics on MnFe_2O_4 was explained based on the formed intermediates, their reactivities, hydrophobicity and to point of zero charges. It has been explored that the reduction efficacy of 4-NP was enhanced on MnFe_2O_4 with the addition of ammonium oxalate and benzoquinone where it was inferior following the addition of tertiary-butyl alcohol. More important correlations concerning the effect of octahedral sites, residual organics, heat of activation (E_a) and activation free energy (ΔG^*) values; determined while the removal of citrate/PVA moieties, on nitroarenes reduction rates were well scrutinized and discussed.

© 2015 Elsevier B.V. All rights reserved.

1. Introduction

The great release of hazardous pollutants into the environment is increasing with the industrialization progression. Hazardous pollutants containing organic nitro compounds are distinctively dangerous because of their toxic and carcinogenic character [1].

Pure pollutants usually decompose at high temperatures, however, solutions of nitro compounds may decompose at much lower temperatures exhibiting large amounts of heat. Amongst these, the aromatic nitro compounds especially nitrophenols are the major pollutants existing in industrial and agricultural waste waters because of their solubility and stability in water [2]. On the other hand, nitroaniline, which dissolves in hot water and ethanol, causes respiratory tract irritation, anoxia due to the formation of methemoglobin and bone marrow abnormalities with damage to blood forming tissues [3]. Because of their dangerous nature,

* Corresponding author.

E-mail address: mohmok2000@yahoo.com (M.M. Mohamed).

nitrophenols and nitroaniline have been arranged as priority pollutants by the U.S Environmental Protection Agency [4]. Besides, picric acid that is used as a primary explosive is highly toxic and dangerous material. Therefore, the removal of such pollutants from industrial waste water is crucial for environmental health. Therefore, many researchers are appointed to develop environmental and clean techniques for the removal of such pollutants from industrial waste water. Many redox processes have been managed for the removal of nitroaromatics such as catalytic moist air oxidation [5], photo-catalytic degradation [6,7], electrochemical processes [8–10], hydrogenation reactions [11,12], etc. An important way to remove nitroaromatics and to get the maximum benefit is to carry out their reduction to aminoaromatics. Aminoaromatics are the most important constituents in the synthesis of many industrial dyes, pharmaceuticals, corrosion inhibitor, photographic developers and some biologically active compounds [13,14]. Many methods are available for the reduction of nitroaromatics to the corresponding aminoaromatics namely electrolytic reduction [15], metal/base reduction [16], homogenous catalysis [17], heterogeneous catalytic hydrogenation [18], photo-reduction [19,20] and use of reducing agents like hydrazine hydrates [21], etc. Nevertheless, these methods are associated with one or more limitations such as problematic in catalyst retrieval, problems concerning discarding metal oxide sludge, time-consuming, hazardous effects of some of the used reagents, carcinogenic and mutagenic effects of hydrazine etc. However, reduction using NaBH_4 was shown to be activated in the presence of suitable catalysts via giving the corresponding hydride [22]. For instance, transition metals in aqueous media produce metal borides in presence of NaBH_4 that reduces nitro aromatics via evolution of H_2 gas and production of hydride ion [23]. For example, Mandlimath and Gopal [24] carried out nitrophenols reduction using NaBH_4 in the presence of group-A (CuO , Co_3O_4 , Fe_2O_3 , NiO) and group-B (TiO_2 , V_2O_5 , Cr_2O_3 , MnO_2 and ZnO) of first row transition metal oxides. The first oxides enhanced the electron transfer process necessary for reduction whereas oxides of group B were inactive. It has also been demonstrated that [25] the catalytic reduction of nitrophenols can be obtained on high precious metals such as gold and silver nanocatalysts. The Au and Ag nanocatalysts those synthesized via different procedures [20,24–25] and showed various morphologies were used to reduce nitroaromatics photo-catalytically based on their surface plasmon resonances phenomena. Du et al. [26] exploited the nanocomposite $\text{Fe}_3\text{O}_4/\text{SiO}_2$ (Ag) of microspheres shape for the reduction of 4-nitrophenol in aqueous medium at room temperature as a magnetic separable catalyst. Ni catalysts were the primer ones on their surfaces nitroaromatics reduction were performed. Lately, Kalbasi et al. [27] examined Nanoparticles–polyvinyl amine/SAB-15 catalyst for fast reduction of aromatic nitro compounds. On the other hand, ferrites of the type MFe_2O_4 with the spinel structure and magnetic properties were also utilized as catalysts for the reduction of nitrophenol. Feng et al. [28] examined the effectiveness of CuFe_2O_4 magnetic nanoparticles for the nitrophenol reduction that has been achieved in presence of 200 equivalent excess of NaBH_4 at the conversion of 95% achieved in 40 s. However, this later catalyst suffers from week stability and hard regeneration. So far very few reports are available where ferrites have been utilized as catalysts for the reduction of aromatic nitrocompounds in presence of NaBH_4 as reducing agent. The use of ferrites as catalysts is very beneficial because of simple and facile synthetic procedure as well as their resistance to severe acidic and basic conditions. Their magnetic nature makes them magnetically separable from the reaction mixture in a convenient manner. Therefore, the present work deals with the investigation of comparative catalytic efficiency of pure ferrites MFe_2O_4 ($\text{M} = \text{Mn}$, Co , Zn) synthesized by sol gel-hydrothermal method in the reduction reaction of nitrophenols (4-nitrophenol and 2,4,6-trinitrophenol) and 4-nitroaniline to the corresponding amino derivatives. The

kinetics of the reduction is also examined. The enhanced reduction efficiency of nanoferrites, effect of residual polyvinyl alcohol used while synthesis on surface, optical properties, point of zero charge and crystallites size has been evaluated in a firm way with the samples catalytic performances. Effects of the addition of some organic moieties on the reduction performances are also well explored.

2. Experimental

2.1. Materials

Ferric chloride, zinc acetate, manganese formate, cobalt chloride, citric acid (99.57%), sodium borohydride (97%), polyvinyl alcohol (PVA, Fluka, M.Wt = 1,250,000) and sodium hydroxide were obtained from Fisher Scientific. 4-nitrophenol; 4-NP (99%), 2,4,6-trinitrophenol; 2,4,6-NP (99%) and 4-nitro-aniline; 4-NA (99%), were purchased from S.D. Fine chemicals. All the chemicals were of analytical grade, commercially available and used without further purification.

2.2. Catalyst fabrication

Nano-ferrites MFe_2O_4 ($\text{M} = \text{Mn}$, Co , Zn) were synthesized employing the sol gel-hydrothermal technique. The stoichiometric amounts of desired metal acetates and citric acid; used to acquire homogenous distribution of the metal ion (in the molar ratio 1:1), were separately dissolved in minimum amounts of distilled water. On the other hand, iron chloride was dissolved in distilled water to give a molar ratio of $\text{Fe}/\text{M} = 2$. After complete dissolution, citric acid solution was poured onto the metal precursors followed by polyvinyl alcohol (PVA, 2 g/90 mL) addition whilst stirring. PVA plays many crucial roles in synthesizing nanoferrites including control of the nanoparticles growth, prevention of agglomeration and production of nanoparticles in uniform shapes [29]. Finally, FeCl_3 solution was poured onto the later mixture followed by stirring for 0.5 h. Addition of NaOH solution in step wise manner till reaching pH equal 12 was attained to the mixture that left under stirring for 1 h. Indeed, condensation reactions are expected to occur between the metal ions and the citrates/PVA to yield a complex or polymer network in a colloidal state known as sol facilitated by NaOH addition, to immediately form gel moieties. The resultant sol–gels were autoclaved for 48 h at 453 K. Finally, the obtained mixtures were washed with distilled water and then annealed in an oven at 573 K for 6 h.

2.3. Physical measurements

2.3.1. X-ray diffraction

X-ray diffraction (XRD) was measured at room temperature by using a Philips diffractometer (type PW-3710). The patterns were run with Ni-filtered copper radiation ($\lambda = 1.5404 \text{ \AA}$) at 30 kV and 10 mA with a scanning speed of $2\theta = 2.5^\circ/\text{min}$. The mean particle size was calculated using the Debye–Scherrer Eq. (1), in which K is a constant equal 0.9, λ is the wavelength of the $\text{Cu K}\alpha$ radiation, β is the half peak width of the diffraction peak in radian.

$$D = \frac{K\lambda}{\beta \cos \theta} \quad (1)$$

2.3.2. FTIR spectroscopy

The Fourier transform infrared (FT-IR) spectra were recorded via a single beam PerkinElmer Spectrometer (RXI FT-IR), with a resolution of 2 cm^{-1} . The samples were grounded with KBr (1:100) so as to form tablets, which mounted into the sample holder in the cavity of the spectrometer. The measurements were recorded at the room temperature in the region $4000\text{--}400 \text{ cm}^{-1}$.

2.3.3. N₂ adsorption

The surface properties namely BET surface area, total pore volume (V_p) and mean pore radius (r) were determined from N₂ adsorption isotherms measured at 77 K using conventional volumetric apparatus. The samples were out-gassed at 473 K for 3 h under a reduced pressure of 10^{-5} Torr before starting the measurement. The total pore volume was taken from the desorption branch of the isotherm at $p/p^0 = 0.95$, assuming complete pore saturation.

2.3.4. Ultraviolet–visible diffuse reflectance spectroscopy

Diffuse reflectance ultraviolet–visible spectroscopy (UV–vis DRS) of the samples was carried out at room temperature using UV–vis JASCO spectrophotometer, V-570, in the range of 200–1000 nm. The UV–vis spectra were processed with Microsoft Excel software, consisting of calculation of the Kubelka–Munk function, $F(R_\infty)$, which was extracted from the UV–vis DRS absorbance. The edge energy (E_g) for allowed transitions was determined by finding the intercept of the straight line in the low-energy rise of the plot of $[F(R_\infty) h\nu]^2$, for the direct allowed transition, vs. $h\nu$, where $h\nu$ is the incident photon energy

2.3.5. Transmission electron microscope (TEM)

TEM micrographs were measured using a FEI; model Tecnai G20, Super twin, double tilt 1010, at an accelerating voltage of 200 kV. The powder samples were put on carbon foil with a microgrid. TEM images were observed with minimum electron irradiation to prevent damage to the sample structure. The elemental compositions of the composite material were investigated by energy-dispersive X-ray attached to the TEM equipment. The average particle diameter (d) was calculated by the following formula:

$$d = \frac{\sum n_i d_i}{\sum n_i} \quad (2)$$

where n_i is the number of particle diameter d_i in a certain range, and $\sum n_i$ is more than 100 particles on TEM images of the sample. Computer-assisted counting of nanoparticle images and automated image analysis based software package including KONTRON KS 400 (Zeiss-Kontron) was used.

2.3.6. Determination of point of zero charge

Batch equilibrium technique [30] was employed to determine pH at the point of zero charge (PZC). Portions of nanoferrite powder were introduced into a known volume (20 mL) of 0.1 mol dm⁻³ KNO₃ solution; as an inert electrolyte, for the purpose of adjusting the ionic strength throughout all the experiments. Initial pH values (pH_{initial}) of KNO₃ solutions were adjusted from ~4.5 to ~11.5 via addition of 0.1 mol dm⁻³ HNO₃ or KOH solutions. Suspensions of different solid to solution ratios (1:100) were admitted to equilibrate for 24 h in a shaker thermostated at 298 K. The suspensions were then filtered and the pH values (pH_{final}) were measured again.

2.3.7. Thermogravimetric analysis

Thermogravimetric and differential thermal analyses (TGA/DTGA) were carried out using Shimadzu-50 thermal analyzer units. The sensitivity of TG and DTGA measurements was 0.01 mg and 25 μ V, respectively. In each run 10 mg of uncalcined sample was heated from 303 K to 1273 K at a heating rate of 2.8 K/min in a current of N₂ flowing at a rate of 30 mL/min.

2.3.8. Magnetic properties

Magnetic measurements were carried out at room temperature using a PMC Micro-Mag 3900 model vibrating sample magnetometer (VSM) equipped with 1 Tesla magnet.

2.4. Kinetic analysis

The thermal data-under investigation was analyzed according to Kissinger equation [31]:

$$\beta \frac{d\alpha}{dt} = A e^{-E_a/RT} f(\alpha) \quad (3)$$

where α is the fraction reacted (alternatively called conversion degree), T is the Kelvin temperature, β is the heating rate ($\beta = dT/dt$, where t is the time), A is the pre-exponential factor, E_a is the activation energy, R is the gas constant and $f(\alpha)$ is the differential form of the reaction model, i.e., a function of α which well fits the experimental data.

The kinetic analysis was performed by means of Software Kinetic program [32], which includes the majority of reaction models, ranging from 1st order, to n th order, nucleation-growth model, as well as the activation energy distribution models, and uses a non-linear regression method to determine the parameters of Eq. (3) to fit the experimental data. To check the presumed invariance of E_a on α , the software Kinetic program performs the isoconversional “model-free” analysis by means of expanded Horowitz–Metzger and modified Coats–Redfern [33]. Multi-heating rate application of the Coats–Redfern equation may be expressed by the equation:

$$\log \left[\frac{\log \{W_f/W_f - W\}}{T^2} \right] = \log \left[\frac{AR}{\theta E^*} \right] - \frac{E^*}{2.303RT} \quad (4)$$

where W_f is the mass loss at the completion of the reaction, W is the mass loss at Kelvin temperature T , R is the gas constant, E^* is the activation energy in kJ mol⁻¹, θ is the heating rate. A plot of the left-hand side of Eq. (4) against $1/T$ gives a slope from which E^* was calculated and A was determined from the intercept.

On the other hand, we applied the Horowitz–Metzger equation [34,35] to the thermal data under study which may be written in the form:

$$\log \left(\frac{W_\infty}{W_r} \right) = \frac{\theta E^*}{2.302RT_s^2} \quad (5)$$

where $T_s = DTG$ peak temperature and $\theta = T - T_s$. A plot of $\log [W_\infty/W_r]$ vs. θ will give a straight line with a slope from which E^* can be calculated. The pre-exponential factor A was calculated by Horowitz–Metzger [34] from the following equation:

$$\frac{E^*}{RT_s^2} = \frac{A \times e - (E^*/RT_s)}{\theta} \quad (6)$$

The activation entropy (ΔS^*), activation enthalpy (ΔH^*) and the activation free energy (ΔG^*) were calculated using the following equations [36]:

$$\Delta S^* = 2.303 \left[\log \left(\frac{Ah}{kT} \right) \right] R \quad (7)$$

$$\Delta H^* = E^* - nRT \quad (8)$$

$$\Delta G^* = \Delta H^* - T\Delta S^* \quad (9)$$

Where k and h are the Boltzmann and Blank constants, respectively. The values of E^* , A , ΔS^* , ΔH^* and ΔG^* for the different decomposition steps are calculated.

2.5. Catalytic reaction

To investigate the catalytic reduction of 4-nitrophenols, 2,4,6-trinitrophenol and 4-nitroaniline, 100 mL of 0.1 mmol aqueous solution of the nitroaromatics was taken in a 250 mL beaker and 12.5 mL of 0.5 M (5 equivalents) of NaBH₄ was added. The latter ratio (NaBH₄/nitro-compounds = 5) was appointed to achieve

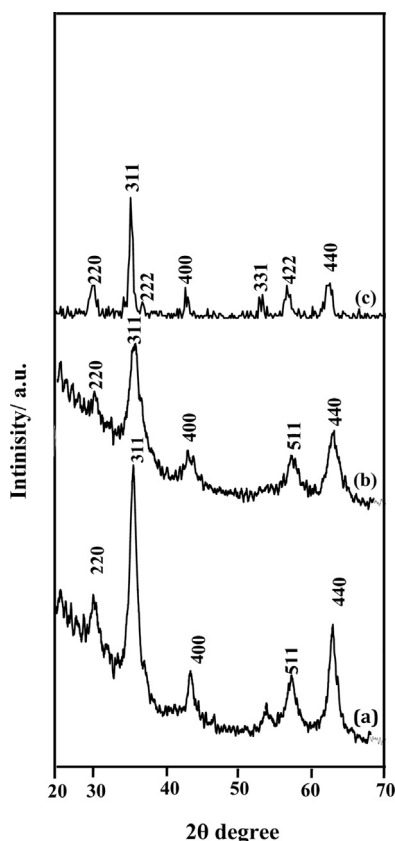


Fig. 1. XRD patterns of (a) MnFe_2O_4 , (b) CoFe_2O_4 and (c) ZnFe_2O_4 samples calcined in air at 573 K.

a green synthesis method. The solution was subjected to constant stirring. With the addition of NaBH_4 , the yellow color of the solution was darkened due to the formation of phenolate ions. A desired amount of MFe_2O_4 ($\text{M} = \text{Mn, Co, Zn}$) nanoferrite catalysts was added; so as to reaching 1 g/L, while stirring and continued at room temperature. The dark yellow color of the solution progressively vanished, demonstrating the reduction of nitroaromatics. The reaction progress was checked via withdrawing samples from the reaction mixture at normal time intervals. The conversion of nitroaromatics to the corresponding aminoaromatics was checked by UV-Visible spectroscopy (a Perkin Elmer Lambda-900) by measuring the absorption maxima corresponding both the reactant and the product. After reaction completion, i.e., after complete disappearance of the yellow color, the catalyst was separated with the help of an external magnet. Detailed determination of GC to accustom the formation of amino-compounds was as follows: 30 mL sample was extracted using 10 mL dichloromethane for three times under acidic (pH 2.0), neutral (pH 7.0), alkaline (pH 12.0) conditions, respectively. The three extracted layers were mixed up, and then dehydrated with anhydrous sodium sulphate under nitrogen atmosphere. Subsequently, the residue was dispersed in 1.0 mL CH_2Cl_2 and 1 μL of the liquid was injected into a capillary column GC Varian 3900. The GC column was operated in a temperature program mode beginning at 40 °C for 3 min, rising by 10 °C/min to 280 °C, and holding at 280 °C for 5 min.

3. Results and discussion

3.1. The structure and morphology of nanoferrites

The purity and crystallinity of as synthesized nanoferrites were examined by XRD and shown in Fig. 1. All the strong sharp

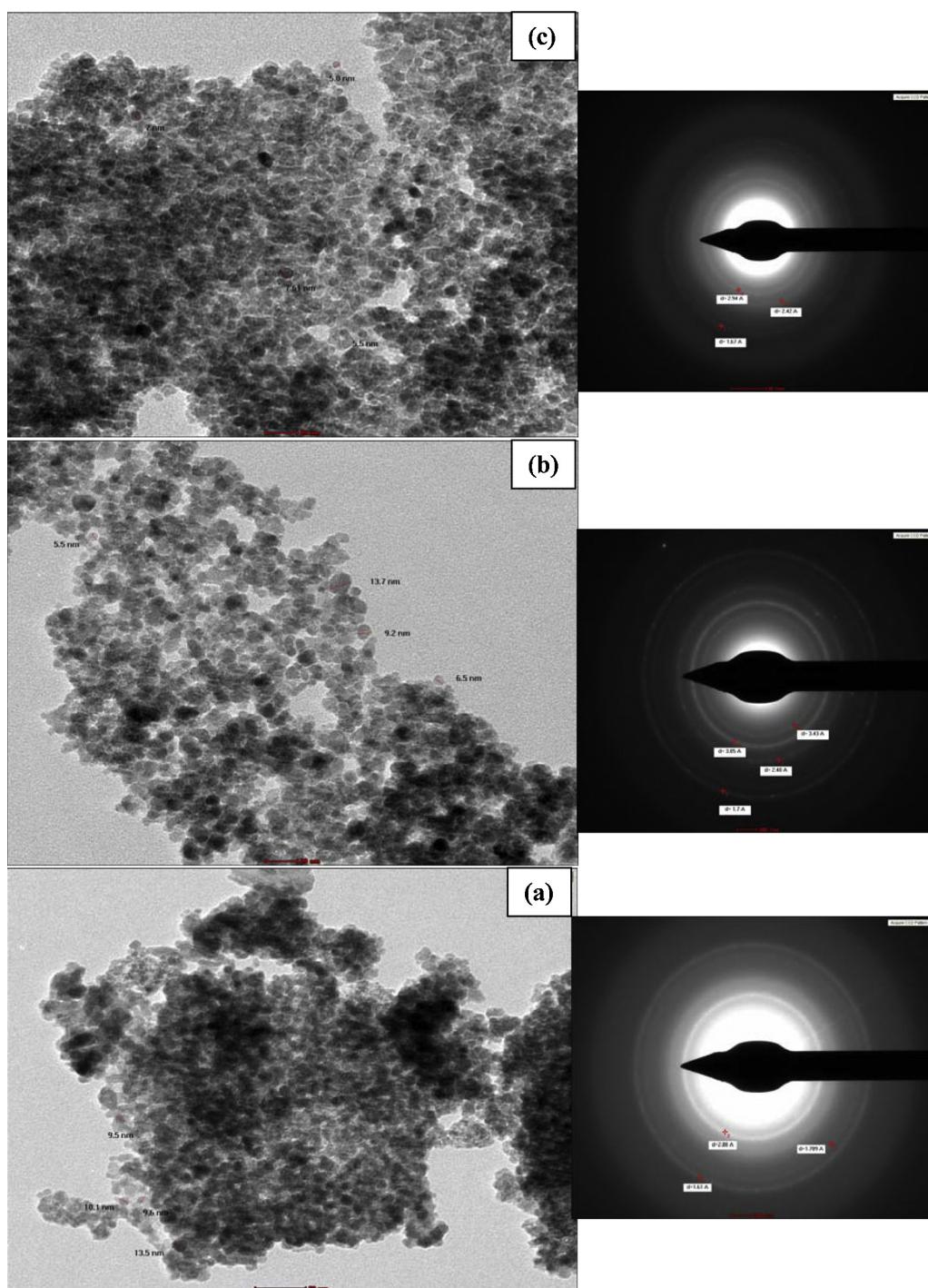
diffraction peaks in CoFe_2O_4 (JCPDS 22-1086), MnFe_2O_4 (JCPDS 73-1964) and ZnFe_2O_4 (JCPDS 22-1012) samples are well indexed respectively, to the corresponding cubic spinel structure and a face-centered cubic (fcc) phase with $\text{Fd}3\text{m}$ space group. The obtained patterns indicate that the synthesized samples are highly crystalline and in single phase without impurities. In conformity, The lattice constant a calculated from the patterns of CoFe_2O_4 , MnFe_2O_4 and ZnFe_2O_4 samples was 8.379, 8.365 and 8.411 Å respectively (Table 1), very close to the reported data ($a = 8.360 - 8.511$ Å) [37]. Increasing the lattice parameter for Zn ferrite is due to increasing the ionic radius of Zn^{2+} (0.82 Å) relative to other metal ions leading to an expansion. Accordingly, this indeed indicates that the sol gel-hydrothermal is a perfect method for the spinel synthesis without extra phases. The morphologies of CoFe_2O_4 , MnFe_2O_4 and ZnFe_2O_4 were characterized by TEM (Fig. 2). The obtained particle size distribution curve (Fig. 2, in-set) of ZnFe_2O_4 revealed a nanocircular structure with an average size of 6.27 nm. The illustrated selected area electron diffraction (SAED) pattern of ZnFe_2O_4 nanoparticles is indexed perfectly to the face centred cubic structure via the existed facets at 2.94, 2.42 and 1.67 Å, in agreement with XRD results. Similarly, the TEM images of CoFe_2O_4 and MnFe_2O_4 those demonstrated high crystalline nanoparticles of spherical shape indicate, respectively average diameters equal 8.72 nm and 10.6 nm. The obtained rings in SAED patterns of later samples are perfectly indexed to highly crystalline pure cubic phase via notifying the facets at 3.43, 3.05, 2.40, and 1.7 Å for CoFe_2O_4 and 2.80, 1.78 and 1.61 Å for MnFe_2O_4 . On the other hand, the EDX spectrum of MnFe_2O_4 (Fig. S1) exhibits that the ferrite is mainly consists of Mn and Fe (with the ratio of 1:2), which was in accord with the theory formula of MnFe_2O_4 . It is evident that our nanoferrites have crystallite sizes lower than other synthesized ones [28,38] notably because our synthesis method has influenced the crystal growth. For verifying that the adopted procedure is highly efficient in forming pure phases at lower temperatures as well as with lower particle domain, TGA kinetic studies are performed.

3.2. Thermokinetic analysis of nanoferrites during their formation

The reaction process of FeCl_3 with $\text{Mn}(\text{HCO}_2)_2$, $\text{Zn}(\text{Ac})_2$ and CoCl_2 in presence of citric acid/PVA was examined by TGA analysis (Fig. 3) with a heating rate equal 2.8 K min^{-1} in air. There are three apparent weight losses in the TGA curves covering the range from room temperature to 1273 K. The first loss at 332 K depicted in Zn, Mn and Co containing samples could be attributed to the removal of physically adsorbed water derived from citric acid decomposition and PVA dehydration. The weight loss corresponds to this first step constitutes 7.20%, 43.88% and 13.26%, respectively. The second step weight loss that correspond to FeCl_3 reaction with zinc acetate and Mn formate dihydrate as well as with CoCl_2 to release of water, carbon oxides and other by-products indicated maxima at 551 K, 642 K and 611 K, respectively. These latter maxima represented respectively, the formation of ZnFe_2O_4 , MnFe_2O_4 and CoFe_2O_4 nanoferrites. The temperatures corresponding to these nanoferrites formation were markedly lower than others synthesized by other techniques [39]. This second stage at 473–673 K showed a decrease in weight loss comprised of 12.43% for ZnFe_2O_4 , 5.30% for MnFe_2O_4 and 0.512% for CoFe_2O_4 due to the elimination reactions occurred between residual acetate group and partially hydrolyzed form of PVA/ citric acid. The third stage indicates weight losses equal 4.09%, 1.31% and 6.27% correspond to ZnFe_2O_4 , MnFe_2O_4 and CoFe_2O_4 in the 769–1231 K range due to simultaneous condensation of the lattice oxygen and formulation of carbon metals/metallic residues. Although the as-synthesized samples calcined at 573 K to form the corresponding pure nanoferrites; as configured by XRD results, some of the maxima derived from DTG curves were exhibited at higher temperatures such as MnFe_2O_4 (642 K) and CoFe_2O_4

Table 1State of spinel ferrite samples as characterized by X-ray diffraction, surface texturing and optical band gap (E_g).

Samples	Data of XRD			Surface texturing				Magnetism data			Band gap (ev)	Average size by TEM (nm)
	Crystal size (nm)	Lattice paramter (Å)	Cell volume (Å) ³	S_{BET} (m ² /g)	S_{ext} (m ² /g)	r_{-} (Å)	V_p^{total} (cm ³ /g)	H_c (Oe)	M_r (emu/g)	M_s (emu/g)		
MnFe ₂ O ₄	2.34	8.365	585.433	67.1	67.1	67.5	0.227	48.0	42.1	135	1.25	10.6
CoFe ₂ O ₄	5.88	8.379	588.352	114	114	34.1	0.194	49.9	40.1	37	0.9	8.72
ZnFe ₂ O ₄	2.58	8.411	595.081	91.6	91.6	35.1	0.160	48.6			1.3	6.27

**Fig. 2.** TEM images and SAED of (a) MnFe₂O₄, (b) CoFe₂O₄ and (c) ZnFe₂O₄ samples calcined in air at 573 K.

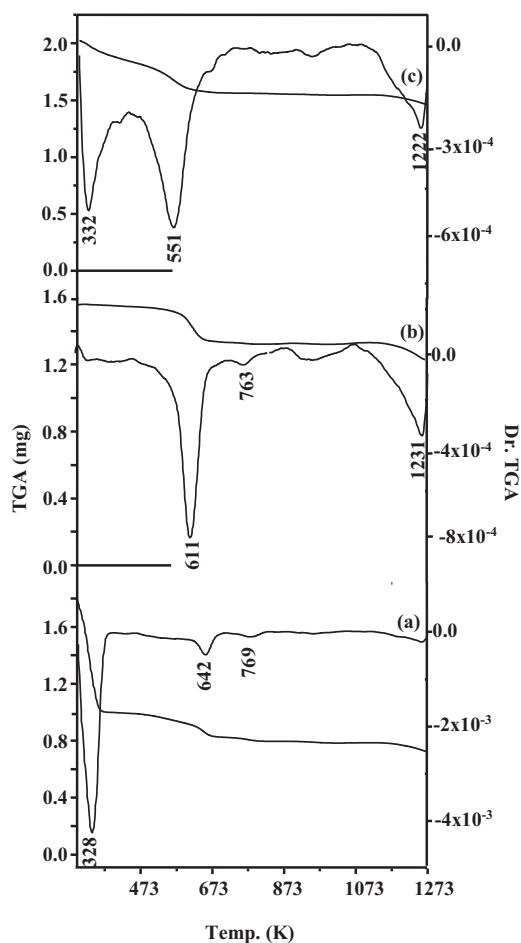


Fig. 3. TG and DTG curves of (a) MnFe_2O_4 , (b) CoFe_2O_4 and (c) ZnFe_2O_4 precursors at a heating rate of 2.8 K/min in static air.

(611 K). This suggests that the changes in the phase transitions temperature are due to the varied interaction of the involved metal ions (Zn, Co and Mn) with PVA/citric, which induce structural modifications. This explains that the gel decomposes suddenly in a single fast step in case of ZnFe_2O_4 (551 K) to form ferrites at comparatively lower temperatures compared to rest of samples. On the other hand, this obtained data declares the presence of residual organics with the spinel forms of MnFe_2O_4 and CoFe_2O_4 .

The kinetic parameters derived via HM method [34] are listed in Table 2. The following remarks are strongly emphasized: (i) the correlation coefficient, r , which was computed using the least square method was in good order and sometimes exceeded 0.99, indicating a good linearity of the experimental data. (ii) the negative ΔS^\ddagger values indicated an ordered activated intermediate in all samples except the second step in case of MnFe_2O_4 that gives a value equal $0.037 \text{ KJ mol}^{-1} \text{ K}^{-1}$ descriptive of the disorder behavior of PVA/citric acid on interacting with Mn precursor. This probably due to the severe water loss (43.8%) occurred for this specific sample at 328 K. The positive values of ΔH^\ddagger mean that the decomposition processes are endothermic in nature. (iii) As shown by Table 2, the E_a values at the corresponding temperatures revealed that the decomposition occurred in the first step; concerned with removal of physically adsorbed water and PVA dehydration, were the least whereas those of second and third steps were the highest. Interestingly, the E_a value of ZnFe_2O_4 formation; second step, was the lowest (63.46 KJ/mol) representing the facile formation of this nanoferrite comparatively under the mentioned experimental conditions. This sample indeed gives a maximum at

551 K lower than other samples comprehending its weak bonding with PVA/citric acid molecules compared with other samples e.g., MnFe_2O_4 (188.57 KJ/mol). (iv) The values of the activation free energy ΔG^\ddagger which increases significantly for the subsequent decomposition stages for all samples indicate the nonspontaneous behavior. This is due to increasing the values of $T\Delta S^\ddagger$ significantly from one step to another and thus overriding the values of ΔH^\ddagger . Increasing the values of ΔG^\ddagger for the subsequent steps of CoFe_2O_4 reflect that the removal rate of citrate/PVA moieties was the lowest in this specific sample comparatively. This may be attributed to the structural rigidity after the expulsion of one species and/or more citrate/PVA, as compared to other samples, which requires more energy, $T\Delta S^\ddagger$, for its rearrangement before undergoing any compositional change. (v) There is no apparent gap in the values of the heat of activation E^\ddagger and the enthalpy of activation ΔH^\ddagger in all nanoferrite samples probably due to the structural packing of the formed PVA/citric acid with nanoferrites does not take much time to form the crystal architecture.

3.3. Surface properties and Point of zero charge effect

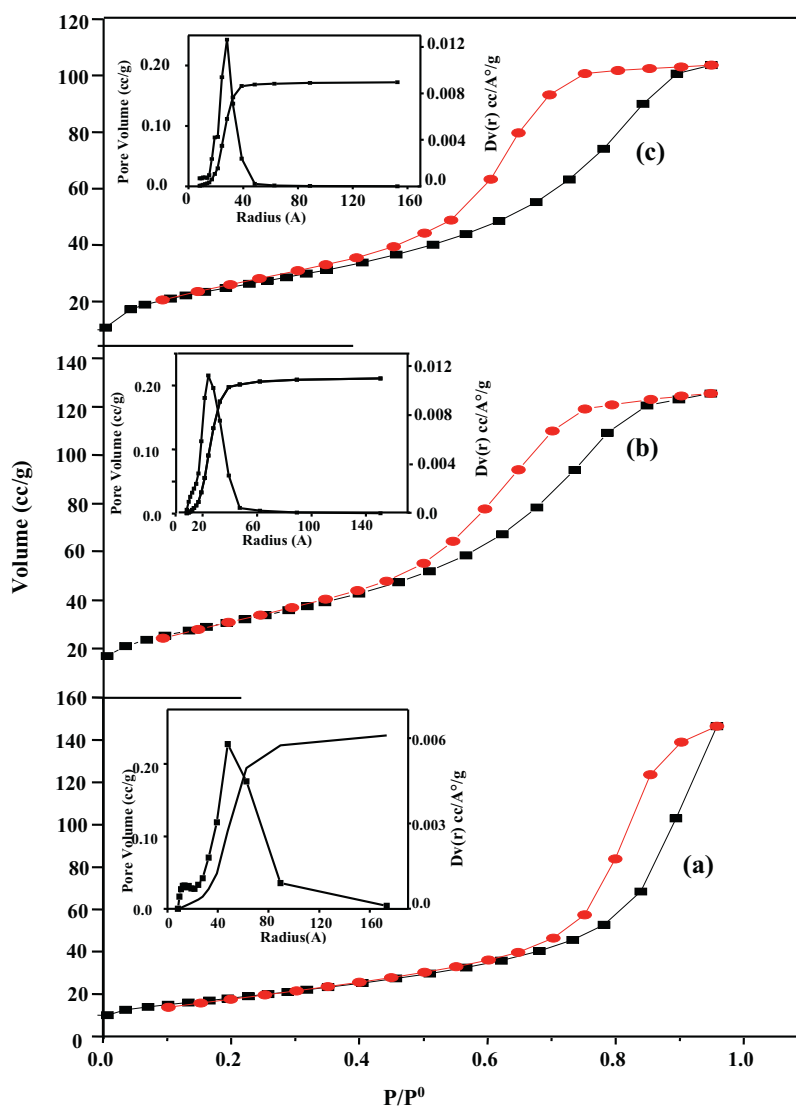
The N_2 adsorption–desorption isotherms for the nanoferrites are shown in Fig. 4 together with the corresponding pore size distribution curves. The N_2 adsorption–desorption isotherms for all of the nanoferrites exhibit type IV isotherm, which are typical of mesoporous materials, with a type H2 hysteresis loop associated to capillary condensation. ZnFe_2O_4 shows broader hysteresis loop than CoFe_2O_4 (Fig. 4) covering the range from $p/p^0 = 0.12$ to 0.95 where the later covers the range from $p/p^0 = 0.22$ to 0.95. This points that ZnFe_2O_4 contains higher percentages of micropore type of pores. On the other hand, MnFe_2O_4 occurs in the pressure range from 0.55 to 0.95 emphasizing the mesoporosity type of pores. The pore size distribution curves displayed unimodal type of pores covering the range from 15 to 50 Å in ZnFe_2O_4 with a maximum distribution at 30 Å where that of CoFe_2O_4 indicates a maximum at 28 Å displayed in the range from 9 to 48 Å. On the other hand, MnFe_2O_4 indicates bimodal distribution at 10 and 60 Å highlighting the increase of the mesoporosity of this sample comparatively. The BET surface area, pore volume and pore diameter of synthesized nanoferrites are given in Table 1. The surface area of nanoferrite catalysts follows the order: $\text{CoFe}_2\text{O}_4 > \text{ZnFe}_2\text{O}_4 > \text{MnFe}_2\text{O}_4$, whereas MnFe_2O_4 indicated the highest pore volume and pore radius values. The reduction in the surface area of ZnFe_2O_4 ($91.6 \text{ m}^2/\text{g}$) compared to CoFe_2O_4 ($114.21 \text{ m}^2/\text{g}$) confirms the presence of residual organics blocking some mesopores in ZnFe_2O_4 ; as will be confirmed from IR results, and probably transferred some of it into micropores; as evident from the isotherm tail of this sample. Whereas, the reduction confirmed in MnFe_2O_4 ($67.1 \text{ m}^2/\text{g}$) is probably due to increasing both pore volume and radius comparatively. Moreover, the marked enhancement in surface area and pore volume of our synthesized nanoferrites compared to those fabricated by others such as pure ZnFe_2O_4 -MM ($11.51 \text{ m}^2 \text{ g}^{-1}$), ZnFe_2O_4 -NP ($3.30 \text{ m}^2 \text{ g}^{-1}$) and hybrid of ZnFe_2O_4 with graphene ($26.35 \text{ m}^2 \text{ g}^{-1}$) was observed [40]. This probably due to the templating route attained via using PVA in creating mesopores based on self-assembly of this nonionic surfactant with the ferrite precursors. The average pore diameter calculated by the Barrett–Joyner–Halenda (BJH) method for the entire nanoferrites indicates a value around 34–35 Å for ZnFe_2O_4 and CoFe_2O_4 and 67.5 Å for MnFe_2O_4 which is clear evidence for the formation of mesoporous structure with uniform size. Indeed, the unique spherical particles with ordered cubic spinel structure and of mesoporous nature may provide more active sites for absorption of nitroarene molecules, resulting in an enhanced catalytic reduction activity especially for MnFe_2O_4 .

The plateau in pH_{final} ($\text{pH}_{\text{initial}}$) curves for nanoferrites indicates PZC variations in the following order: $\text{CoFe}_2\text{O}_4 > \text{MnFe}_2\text{O}_4 > \text{Zn}$

Table 2

Decomposition temperature, order and activation parameters of spinel ferrite prepared by hydrothermal methods [34].

Samples	Step	T/K	Wight loss	Assignment	A/S^{-1}	$E/KJ\ mol^{-1}$	R^2	$\Delta H^*/KJ\ mol^{-1}$	$\Delta S^*/KJ\ mol^{-1}K^{-1}$	$\Delta G^*/KJ\ mol^{-1}$
$MnFe_2O_4$	First	328	43.88%	Phys. ads. H_2O	2.05×10^3	30.082	0.986	27.3523	-0.163	80.927
	Second	642	5.30%	Resid. acetate group and partially hydrolyzed form of PVA	1.16×10^{14}	188.579	0.947	183.236	0.037.114	159.379
	Third	769	6.27%	Carbon metals/metallic residues	6.38×10^{-9}	126.747	0.998	120.350	-0.428	450.317
$CoFe_2O_4$	First	611	13.26%	Phys. ads. H_2O	0.191	9.465	0.971	4.379	-0.264	166.152
	Second	763	0.512%	Resid. acetate group and partially hydrolyzed form of PVA	9.96×10^7	139.431	0.998	133.083	-0.080	194.533
	Third	1231	1.31%	Carbon metals/metallic residues	1.30×10^{13}	313.216	0.916	302.974	-0.522	946.819
$ZnFe_2O_4$	First	332	7.20%	Phys. ads. H_2O	1.58×10^3	29.839	0.988	27.075	-0.165	82.081
	Second	551	12.43%	Resid. acetate group and partially hydrolyzed form of PVA	2.57×10^4	63.466	0.961	58.880	-0.146	139.683
	Third	1222	4.09%	Carbon metals/metallic residues	2.97×10^{11}	253.546	0.993	243.385	-0.477	826.816.9

**Fig. 4.** N₂ adsorption-desorption isotherms and corresponding pore size distribution curves of (a) MnFe₂O₄, (b) CoFe₂O₄ and (c) ZnFe₂O₄ samples calcined in air at 573 K.

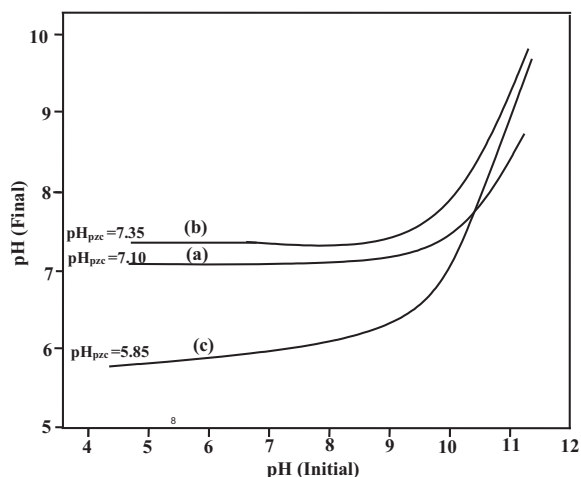


Fig. 5. pH_{final} as a function of $\text{pH}_{\text{initial}}$ for (a) MnFe_2O_4 , (b) CoFe_2O_4 and (c) ZnFe_2O_4 samples performed in presence of $0.1 \text{ mol dm}^{-3} \text{ KNO}_3$ for detecting pH_{ZPC} .

Fe_2O_4 (Fig. 5). The CoFe_2O_4 and MnFe_2O_4 show large buffer capacity covering the pH range from ~ 4.5 to ~ 11 having almost the same value of pH_{ZPC} at 7.35 and 7.10, respectively. However, ZnFe_2O_4 shows step wise increase in the later margin unlike its pH_{ZPC} that configured at 5.58. Accordingly, an expected increase in the reduction rate of nitroarenes on our synthesized nanoferrites could be due to exceeding the adsorption of nitrocompounds onto nanoferrite surfaces facilitated by electrostatic forces.

3.4. FTIR Study

FTIR spectra are employed to verify the nanoferrites formation after calcining at 573 K in the wavenumber range of $400\text{--}4000 \text{ cm}^{-1}$. All the spectra show (Fig. 6) two principle absorption bands in the range of $400\text{--}600 \text{ cm}^{-1}$. These two vibrational bands correspond to Fe–O and M (Zn, Co and Mn)–O assigned respectively, to intrinsic lattice vibrations of octahedral ($412\text{--}423 \text{ cm}^{-1}$) and tetrahedral coordination ($565\text{--}593 \text{ cm}^{-1}$) in the spinel structure [41]. Shifting the latter into longer wavenumbers than that of the former was due to shortening the bond length in tetrahedral structure than that in octahedral one. The stretching vibration of the Co–O (593 cm^{-1}) group exhibited a significant shift toward high wavenumbers compared to other tetrahedral vibrations ($559\text{--}565 \text{ cm}^{-1}$), suggesting a strong hybridization between Co and Fe while forming CoFe_2O_4 . This was in part due to decreasing the ionic radius of Co^{2+} as well as increasing its electronegativity (1.88) compared to rest of metals. This also specifies that more Co^{2+} ions move to tetrahedral positions. On the other hand, increasing the ionic radius of Zn^{2+} ions makes the Fe^{3+} ions migrate to the octahedral sites, and consequently decreases the tetrahedral vibration frequency (559 cm^{-1}), to be the lowest comparatively. Conversely, migration of the Fe^{3+} ions to the octahedral site increases the octahedral vibration frequency (423 cm^{-1}). The bands with peaks in the range of $1039\text{--}1056 \text{ cm}^{-1}$ and $875(877) \text{ cm}^{-1}$ were assigned, respectively to the C–O stretching vibrations and to C–C stretching vibrations. The bands in the range of 1428 to 1431 cm^{-1} are associated with C–H bending vibration of methylene groups whereas those localized at $\sim 1630 \text{ cm}^{-1}$ and $\sim 3432 \text{ cm}^{-1}$ were associated to the deformation of H_2O vibration and O–H stretching vibration, respectively [42]. This suggests that thermal treatment at 573 K; as performed to our samples, did not remove all organics/PVA moieties however, residual carbonaceous compounds were exposed on all ferrite surfaces. It seems also from the spectra that MnFe_2O_4 has the lowest band intensities occurred in the $800\text{--}4000 \text{ cm}^{-1}$ range revolving that it contains the lowest carbonaceous compounds as

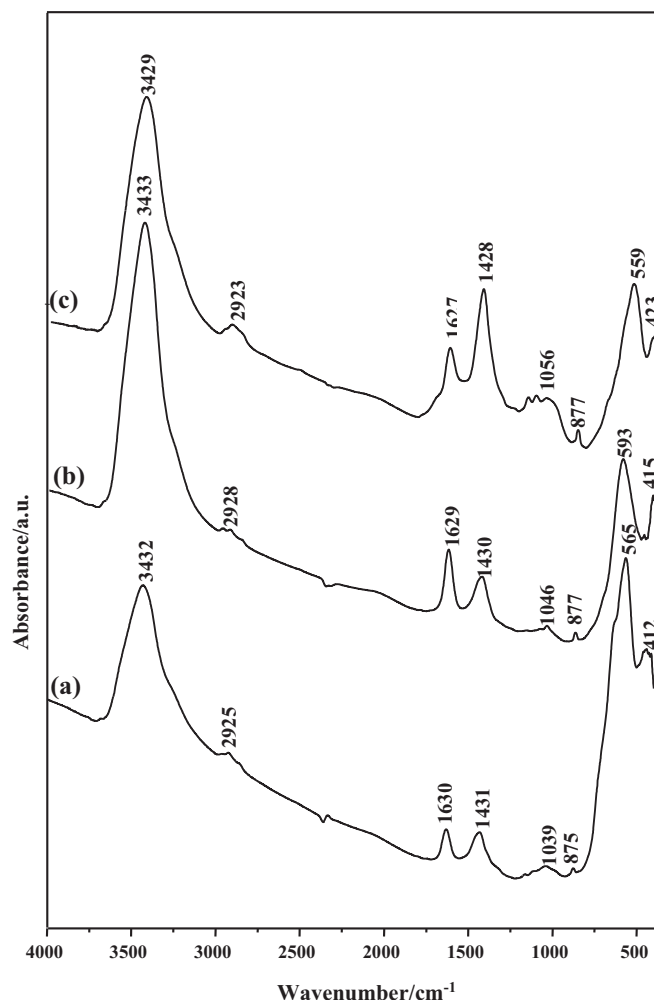


Fig. 6. FT-IR absorbance spectra of (a) MnFe_2O_4 , (b) CoFe_2O_4 and (c) ZnFe_2O_4 samples calcined in air at 573 K.

well as water of hydration probably due to decreasing its ionic radius (70 pm).

3.5. Magnetic properties

The magnetization hysteresis loops recorded at room temperature for nanoferrite samples are shown in Fig. S2. The measured values of the saturation magnetization (M_s), remnant magnetization (M_r) and coercive field (H_c) for all nanoferrites are listed in Table 1. The values of $M_s = 135 \text{ emu/g}$, $M_r = 42.1 \text{ emu/g}$ and $H_c = 48.0 \text{ Oe}$ are observed for the MnFe_2O_4 sample. The saturation magnetization M_s of CoFe_2O_4 was found to equal 37 emu/g much lower than that of MnFe_2O_4 . Increasing the M_s magnetization [43] of later sample than that of the former is due to the misbalance of Fe^{3+} ions in octahedral (B) and tetrahedral (A) sites, super-exchange interactions and the non-collinear nature of moments in the B-site. The higher coercivity value of CoFe_2O_4 (3986 A/m) than MnFe_2O_4 (3882 A/m) and ZnFe_2O_4 (3874 A/m) may be due to the higher magnetocrystalline anisotropy of cobalt cations compared to zinc and manganese cations. The decrease in magnetism of ZnFe_2O_4 probably because Zn^{2+} ions occupy tetrahedral sites and Fe^{3+} ions reside in octahedral sites, besides Zn^{2+} ions are non-magnetic in nature. Consequently, the interactions between Fe^{3+} ions in the octahedral sites are too weak to be important (the B–B interaction is weak in ferrites), hence the magnetization of ZnFe_2O_4 nanocrystals is small. It has been acknowledged that the M_s and H_c values of nano-

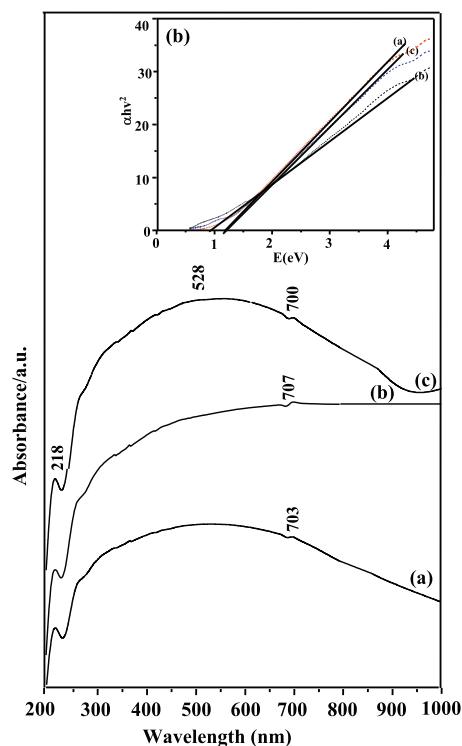


Fig. 7. Diffuse reflectance vs. wavelength for (a) MnFe_2O_4 , (b) CoFe_2O_4 and (c) ZnFe_2O_4 samples calcined in air at 573 K. The inset shows the graphical representation of $(F(R)hv)^2$ vs. hv .

ferrites are quite smaller than in the bulk specimens [44–45] and since ZnFe_2O_4 indicated the lowest crystallite size it presented the lowest magnetization. The decrease of M_s in CoFe_2O_4 nanoparticles is likely due to the canted spins in the surface layers, which is caused by the lack of oxygen mediating super exchange mechanism near the subsurface [46]. It can also be attributed to the enhancement of the surface barrier potential resulted from the distortion of crystal lattice caused by the atoms deviating from normal positions in the surface layers [46]. These effects were getting more intense as the crystal size of the nanoparticles become smaller due to increasing the surface/volume ratio. Lowering the number of magnetic domains and the rate of alignment of the spins with the applied field in the nanoferrite can also affect M_r and M_s values. The macromolecules of PVA is regarded as non-magnetic islands separating the magnetic domains thereby decreasing (M_r) and (M_s) of CoFe_2O_4 that owned appreciable amounts of residual organics comparatively, as devoted from IR and surface results. However, low value of M_r/M_s of nanoferrites can be accounted for by the hysteresis properties of ferrites at low temperature being mainly determined by their surface anisotropy, resulting from surface spin disorder (spin canting) rather than cubic anisotropy.

3.6. Optical study

In order to elucidate the optical response and to determine the band gaps of the nanoferrite samples, UV–visible diffuse reflectance spectroscopy (UV–vis DRS) was carried out, and the results are depicted in Fig. 7. The spectral reflectance was measured in the wavelength range of 200–1000 nm. Although the spectral shapes are generally same, there are prominent differences in the reflection edges. All the samples exhibit a band at 218 nm together with a broad one at 270 nm. These bands are respectively assigned to π – π^* and n – π^* transitions emphasizing the presence of residual organics. An apparent enhancement of the absorption throughout the visible-light region is observed with for all samples till

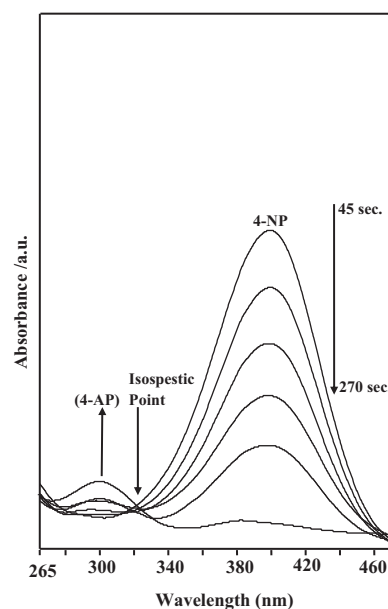


Fig. 8. UV–vis absorption spectra of the reduction of 4-NP using MnFe_2O_4 : conditions: 100 mL 4-NP conc. 0.1 mmol L^{-1} , 12.5 mL NaBH_4 conc. 0.5 M, 100 mg (1 g/L), $T = 298 \text{ K}$

1000 nm. This probably correlated to the exhibited dispersion and to the strong interaction between M (Zn, Co, Mn)–O and Fe–O; as evidenced previously using XRD and IR results. The absorption shoulders of the nanoferrite spectra in the visible regions (500–750 nm) may be attributed to the electron excitation from the O^{2-} p level into the Fe 3d level for spinel-type compound [47]. The absorption intensity of the nanoferrites ZnFe_2O_4 was extremely enhanced compared to other samples to be in the order: $\text{ZnFe}_2\text{O}_4 > \text{CoFe}_2\text{O}_4 > \text{MnFe}_2\text{O}_4$. This was due to the good dispersion of ZnFe_2O_4 as well as to the decreased crystallites size; that resulted in quantum confinement effects [48], comparatively as derived from TEM observation. The facile formation of ZnFe_2O_4 and the exhibited decreased crystallites size could be responsible for increasing the electronic density and thus increasing the absorption intensity.

In order to determine E_g , we have analyzed the measured absorption spectra of the studied nanoferrites by calculating the absorption edge based on the following approximation (inset Fig. 7):

$$F(R)hv = A(hv - E_g)^n \quad (10)$$

The values of optical transition obtained by extrapolating the straight line portion to energy axis at zero absorption coefficients give the direct optical band gaps. In particular, we found that E_g decreases in the following sequence: ZnFe_2O_4 (1.3 eV) $>$ MnFe_2O_4 (1.25 eV) $>$ CoFe_2O_4 (0.9 eV). These results indicate the capability of later samples for capturing visible light than corresponding ones synthesized by different methods as well as exceeding TiO_2 photocatalytic nanoparticles [49]. Smaller band gap value was clearly observed for the nanoferrite CoFe_2O_4 . However, this later sample indicates lower absorption intensity than ZnFe_2O_4 . Indeed, this is because Co is associated with excess electrons; not stable as half-filled (Mn) or completely filled (Zn), and can easily excited when coupled with Fe ions and exposed to photo-irradiation. Then it can be excited to inject electrons into the conduction band of Fe–O. The evolution of additional sub-band-gap energy levels that are induced by the abundant surface and interface defects in the agglomerated nanoparticles also decreases E_g value. The inverse relationship of band gap (1.3 eV) with particle size (6.27 nm) for ZnFe_2O_4 (Table 1) was attributed to the defects or due to change in hybridization with

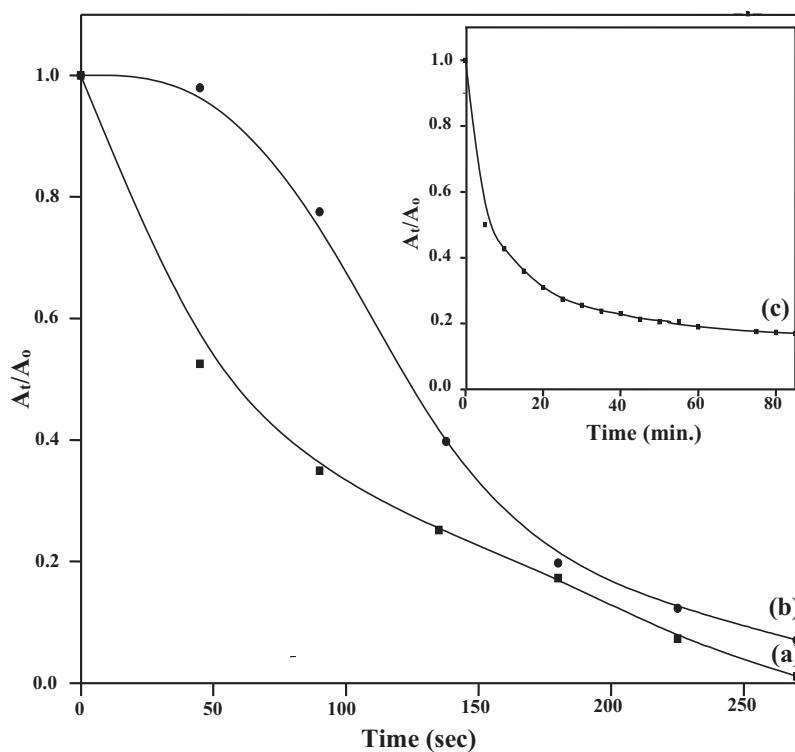


Fig. 9. The change in the concentration of 4-NP with time in the reduction of 4-NP by MnFe_2O_4 in the presence of aqueous NaBH_4 . Reaction conditions: 100 mL 4-NP of conc. 0.1 mmol L^{-1} , NaBH_4 conc. Of 0.5 M, 0.1 g catalyst, $T = 298 \text{ K}$.

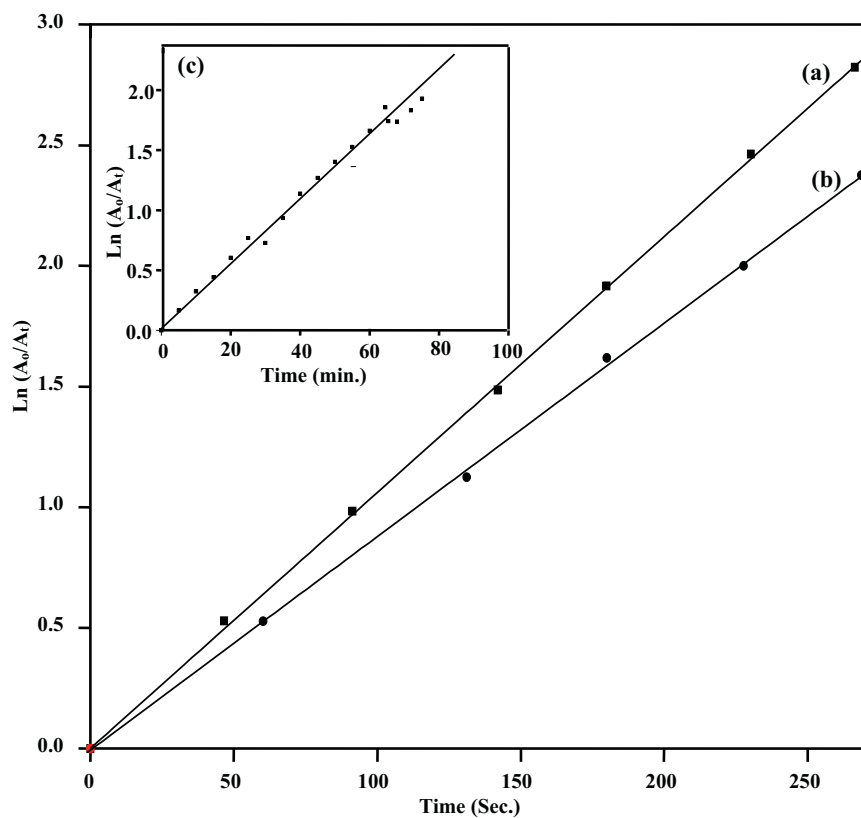


Fig. 10. Plots of $\ln(A_t/A_0)$ vs. time for the reduction of 4-NP in the presence of (a) MnFe_2O_4 and (b) CoFe_2O_4 and in set (c) ZnFe_2O_4 samples calcined in air at 573 K. Reaction conditions: 100 mL 4-NP of conc. 0.1 mmol L^{-1} , NaBH_4 conc. Of 0.5 M, 0.1 g catalyst, $T = 298 \text{ K}$.

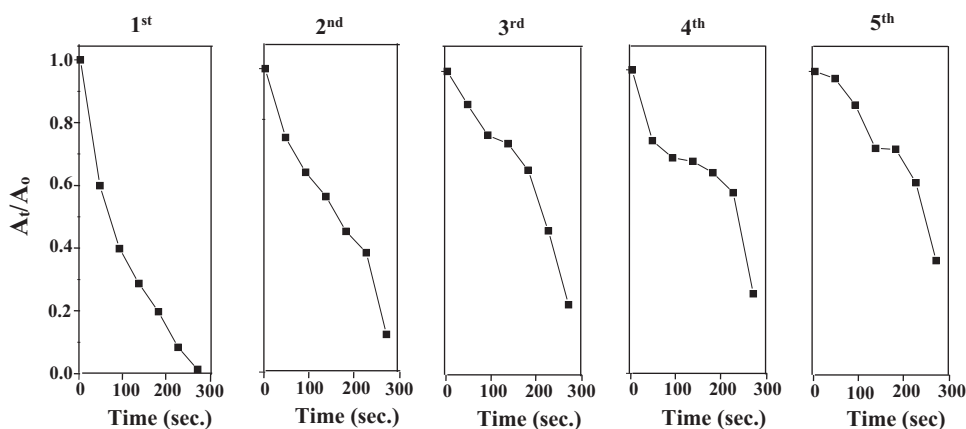


Fig. 11. Repeated cycles up to 5 times illustrating the reduction of 4-NP over MnFe_2O_4 . Reaction conditions: 100 mL 4-NP of conc. 0.1 mmol L^{-1} , NaBH_4 conc. of 0.5 M , 0.1 g catalyst, $T = 298 \text{ K}$.

the change in cell volume; and this specific sample has shown the highest cell volume. The as-prepared materials displayed excellent absorption in the visible region justifying their optical applications.

3.7. Catalytic reduction of nitroarenes compounds

The reduction of 4-NP over the nanoferrite samples in the presence of NaBH_4 was previously investigated on similar samples for the useful production of 4-AP [50–51]. However, our synthesized samples showed comparatively fascinating higher performances even under dark conditions. This reaction was used as a model reaction not only to examine surface texturing and the effect of varying parameters while synthesizing ferrite nanoarchitectures but also investigating the effects of structural changes while nanoferrites syntheses on their catalytic performances. It is observed that when NaBH_4 solution was added to the 4-NP solution, the color of the solution was intensified via giving a peak maximum at $\lambda = 401 \text{ nm}$, indicative of formation of 4-nitrophenolate ions. This solution was stable for hours in absence of any catalyst emphasizing that no hydrogenation reaction took place and rather confirm that this reaction is preceded catalytically. Interestingly, after the addition of nanoferrites to the solution containing 4-NP + NaBH_4 ; while stirring in the dark, there was a continuous fading of the yellow color until vanishing. This indeed occurs via a decrease in the absorption peak of max. at 401 nm with simultaneous evolution of that 300 nm due to 4-AP formation, Fig. 8. This Figure indicates the reduction that occurred on MnFe_2O_4 takes place and accomplished in 270 s , the fastest ever reduction reaction accomplished so far under dark condition on similar samples. The UV–vis spectra show an isosbestic point (Fig. 8), 320 nm), illustrating that the catalytic reduction of 4-NP yields only 4-AP without by-products and proceeds via only one consistent mechanism [52]. Plotting A_t/A_0 vs. time (Fig. 9) indicates an abrupt decrease in the concentration of 4-nitrophenolate ion in the first 90 s of the reduction in presence of MnFe_2O_4 surpassing that of CoFe_2O_4 probably due to the facile evolution of H_2 over the former, comparatively. The inset Figure shows that the nitrophenolate color still exists till 80 min reaction time in case of ZnFe_2O_4 giving reduction conversion comprised of 80% . Plotting $\ln A_0/A_t$ vs. time (sec) indicates straight lines (Fig. 10) with slopes representing reaction rate constants. These lines indicate that this reduction reaction follows pseudo-first order rate kinetics. The rate constant values performed at 298 K were in the order: MnFe_2O_4 (0.011 s^{-1}) > CoFe_2O_4 (0.0089 s^{-1}) > ZnFe_2O_4 (0.0271 min^{-1}). The inset Figure represents ZnFe_2O_4 nanocatalyst signifying the disappearance of 4-NP color in minute's reaction time not in seconds as depicted for Mn and Co ferrites. Indeed, it is clarified that the cat-

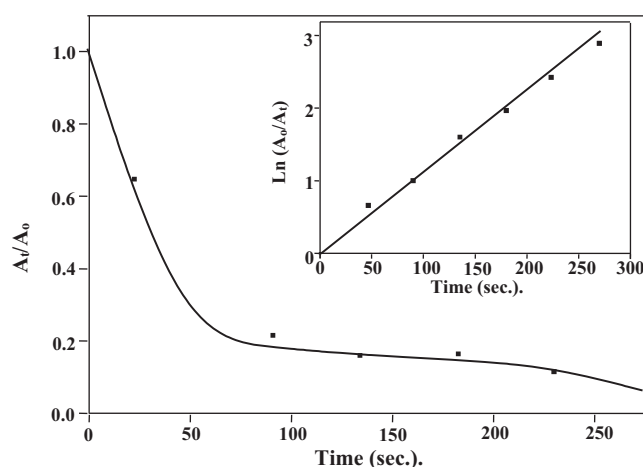


Fig. 12. (a) The change in the concentration of picric acid reduction with time in presence of MnFe_2O_4 catalyst, and in-set is the $\ln A_0/A_t$ vs. time of the same graph. Reaction conditions: 100 mL 4-NP of conc. 0.1 mmol L^{-1} , NaBH_4 conc. Of 0.5 M , 0.1 g catalyst, $T = 298 \text{ K}$.

alytic reduction performance of later nanoferrites exceeded that of ZnFe_2O_4 and MnFe_2O_4 surpassed that of CoFe_2O_4 by a factor of 1.24. Based on the experimental results, one can attribute the increase of the reduction rate of MnFe_2O_4 was not due to decreased crystallites size and surface area values but to the increased pore radius and pore volume values. Accordingly, based on the committed high catalytic potential of MnFe_2O_4 , we chosen it to perform some further reactions. The rate constants obtained for the reduction of 4-nitrophenol via our synthesized nanoferrites were markedly higher as compared to those mentioned in literatures where expensive metal composites were used as catalysts [14,23,51]. Furthermore, the facile procedure employed in this work in synthesizing magnetically separable nanoferrites is a good approach for alternative catalysts for nitrophenols reduction. To explore the applicability of the MnFe_2O_4 catalyst and its reuse, cycles of newly catalyst were tested for the reduction of 4-NP (Fig. 11). Experiments were performed where the nanocatalyst MnFe_2O_4 was recovered and reused without any treatment via keeping all other parameters constant. The results revealed that MnFe_2O_4 shows a very good activity for five catalytic runs with a small loss in the 4-NP conversion. The conversion of 4-NP after the fifth run maintains activity as high as 75% concluding that the MnFe_2O_4 catalyst possesses reasonable stability, high magnetically recycled process and potentiality for practical applications. After recycling tests, MnFe_2O_4 is still in-contact after

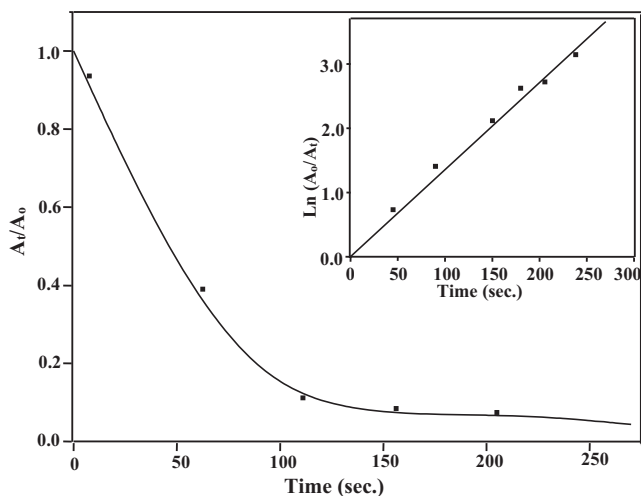


Fig. 13. (a) The change in the concentration of p-nitroaniline reduction with time in presence of MnFe_2O_4 catalyst in the presence of aqueous NaBH_4 with reduction, and the in-set is $\text{Ln } A_0/A_t$ vs. time of the same graph. Reaction conditions: 100 mL 4-NP of conc. 0.1 mmol L^{-1} , NaBH_4 conc. Of 0.5 M , 0.1 g catalyst, $T = 298 \text{ K}$.

five round of reuse, guaranteeing their excellent recyclability and stability in the reaction medium under a strong reducing atmosphere. Performing IR spectra for MnFe_2O_4 after the fifth run (Fig. S3) indicate no changes in the bulk structure of the ferrite highlighting its stability. We traced no any Fe leached in the reacting solution after finishing the reaction comprehending that the catalytic activity of the ferrite is the one responsible for the activity.

The reduction of 2,4,6-NP and 4-NA was also achieved using the nanocatalyst MnFe_2O_4 under similar reaction conditions. 2,4,6-NP shows absorption peak at 355 nm in the UV-vis spectrum. With the catalyst addition, the yellow color of the reaction mixture started fading and the absorption intensity of the peak at 355 nm started decreasing illustrating the reduction of 2,4,6-NP to 2,4,6-AP via existence of a new peak at 299 nm . The reaction was fast and completed in 270 s with rate constant equal 0.01134 s^{-1} (Fig. 12). Similarly, 4-NA absorbs at 382 nm in the UV-vis spectrum and the progress of the reaction was followed via existence of a new peak at 304 nm representing the corresponding amino-compound. The percent conversion for the reduction of 4-NA using MnFe_2O_4 seen in Fig. 13; and completed in 270 s , indicated rate constant equal 0.01355 s^{-1} (in-set Fig. 13).

It can be seen that the rates of reduction of the three of nitro-aromatics performed using MnFe_2O_4 followed the order; 4-NA (0.01355 s^{-1}) > 2,4,6-NP (0.01134 s^{-1}) > 4-NP (0.01061 s^{-1}). It has been acknowledged from literatures [40] that the reduction reaction proceeds via formation of nitrophenolate ion as an intermediate in NPs or via hydroxylamine in 4-NA. The order of reactivity of nitro-aromatics can be explained on the basis of two factors namely the formation of intermediates and their reactivity. For the formation of nitrophenolate ion, the acidic strength for example of nitrophenols plays an important role where NaBH_4 acts as a Lewis base. The order of acidic strength of the nitroaromatics is 2,4,6-NP > 4-NA > 4-NP and the stability of nitrophenolate ions follow the same order. This is due to the fact that in 2,4,6-nitrophenolate ion, the -ve charge of oxygen is delocalized through the benzene ring that stabilized via resonance besides inductive effect of nitro groups those further contribute to the facile liberation of H^+ ion. However, exceeding the reduction rate of 4-NA on MnFe_2O_4 compared to other nitroaromatics could be due to the electron donating ability of NH_2 as well as due to decreasing the electronegativity of nitrogen in aniline moieties compared

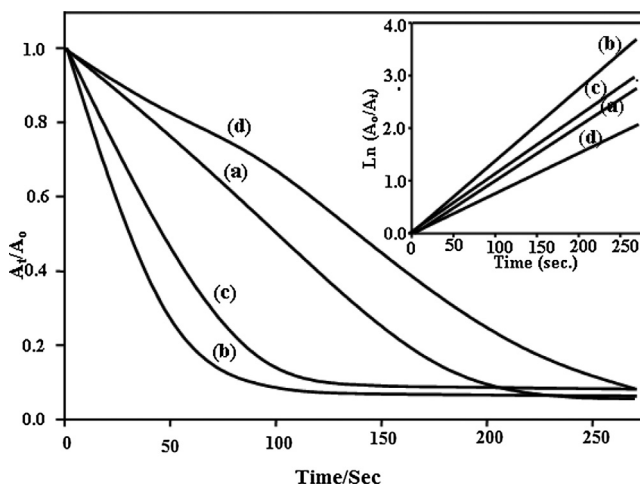


Fig. 14. Effects of the addition of ammonium oxalate, benzoquinone, and tertiary-butyl alcohol on the reduction behaviour of 4-NP in presence of MnFe_2O_4 catalyst where (a) without additives, (b) ammonium oxalate (c) benzoquinone, (d) tertiary-butyl alcohol and the in-set figure represents the corresponding $\text{Ln } A_0/A_t$ vs. time. Reaction conditions: 100 mL 4-NA of conc. 0.1 mmol L^{-1} , NaBH_4 conc. of 0.5 M , 0.05 g catalyst, $T = 298 \text{ K}$.

to oxygen of hydroxyl group in nitrophenol compounds and thus nitrophenolate ions. Also picric acid suffers from steric hindrance upon orientation on the catalyst surface rather than 4-NA. In these nitroaniline molecules, the lone pair of electron of the amino nitrogen atom is attracted toward the strong electron withdrawing NO_2 groups resulting in a resonating structure. Hence, the amino nitrogen becomes positively charged in nitroaniline by which an electrostatic interaction with MnFe_2O_4 at the pH_{ZPC} equal 7.10 is expected. It wise reporting that nitroarenes solution acquire alkalinity in the pH range 9.6 – 9.95 while performing the reduction reactions. Accordingly, at later margin MnFe_2O_4 acquires negative charges on its surface and thus an expected electrostatic repulsion e.g., between the ionized 4-nitrophenolate ions and the ferrite surfaces can be presumed. Conversely, electrostatic attraction is likely between residual positive charges exposed on nitroaniline and those of negative ones created on ferrites surface during interaction. Indeed, the 4-nitrophenolate molecules have an additional -OH group of activating character, which partly reduces the effect of NO_2 group increasing its dispersive interactions with MnFe_2O_4 however, the residual positive charges on 4-NP groups are lower than those on 4-NA ones. Accordingly, the enhanced electrostatic interaction between MnFe_2O_4 with the residual positive charges created on 4-NA exceeded that with 4-NP facilitated the reduction of the former than that of the later. Increasing the reaction rate of MnFe_2O_4 with nitroaniline than with 4-nitrophenol is also due to their hydrophobicity determined by their solubilities: (cs. 4-NP = 0.087 mol/L , cs. NA = 0.015 mol/L), and the effect of adsorbate functional groups and their specific interactions with the active sites of nanoferrite surface. However, the significance that ZnFe_2O_4 presented lower activity although its surface acquires negative charge at solution pH values greater than the PZC; as other ferrites, might be due to this former ferrite will take much time to reorganize its surface due to lowering its pH_{ZPC} (5.7) and to increasing the Zn^{2+} ions size that induces an increase in lattice parameter values and thus increases the long-range electron transfer between Fe^{2+} – Fe^{3+} ions. Accordingly, increasing the reduction rate of nitroarenes on CoFe_2O_4 and MnFe_2O_4 than on ZnFe_2O_4 is presumably due to exceeding the adsorption of nitrocompounds on former ferrites than that on the later facilitated by electrostatic forces.

3.8. Effects of additives on the catalytic reduction of 4-NP

The effects of the addition of ammonium oxalate; AO, benzoquinone; BQ, and tertiary butyl alcohol; TBA, on the catalytic reduction of 4-NP over MnFe_2O_4 have been investigated under the same experimental conditions. It has been shown that the reaction was very fast to be followed during adding up some additives so, we decreased the catalyst weight into 0.05 g. Fig. 14 presents the effects of the mentioned additives with reference to the absence of any additives on a sample consisted of the catalyst and 4-NP. A significant enhancement was obtained for the reduction of 4-NP on MnFe_2O_4 in presence of AO and BQ whereas TBA stimulates a decrease in activity. The in-set in Fig. 14 that shows the relation between $\ln A_0/A_t$ vs. time (sec) indicates rate constants in the order: 0.01366 s^{-1} (AO) > 0.01192 (BQ) > 0.0112 s^{-1} (without) > 0.0077 s^{-1} (TBA). Evidently, both AO and BQ are indispensable for the catalytic reduction of 4-NP over MnFe_2O_4 . As mentioned in literatures, [53] AO and BQ are respectively, used as efficient scavengers for holes and oxygen peroxide radicals; O_2^- , under the photocatalytic action. However, increasing the activity following the addition of latter organics highlights the independence of the reaction on light. For verification, exposing the reaction to both UV and Visible lamps indicates no change in the activity reflecting that it has nothing to do with light capturing abilities of these materials. Accordingly, the significant increase in the activity during for example the addition of AO, is due to the high polarity of oxalate groups ($-\text{C}_2\text{O}_4^{2-}$), which tend to be at the surface of the catalyst particles oriented toward the aqueous phase (nitrocompounds–water interface). The oxalate groups self ionization promotes the catalyst particle surface to acquire –ve charges. Indeed, the catalyst particles acquire extra –ve charges came from the nitroaromatics pH, as mentioned previously. Accordingly, the –ve charges exposed on ferrites nanoparticles impart a high stability, via repelling occurred between nanoferrites and oxalates due to like charges. This may induce the homogeneous diffusion of NaBH_4 into the nitrocompounds stuck into the ferrite surface and hence affects greatly the reduction reaction. On the other hand, AO has acknowledged an excellent reduction ability. On the other hand, benzoquinones are suggested to be dominant redox-active moieties [54], by which redox potentials are varied depending on pH changes due to the coupled electron- and H^+ -transfer. It works as interfacial-mediator to optimize the charge carriers transfer pathway for improving the reduction activity of nanoferrites toward the target nitroaromatics. Indeed, weakening the acidity of tertiary-butyl alcohol decreases the H donor ability and also delayed the charge transfer to nitro compounds because of its bulky nature. Thus, the low release of H protons and the bulky nature of TBA influenced the activity.

3.9. Comparison of the reduction activity

It has been acknowledged from literatures that the mechanism of nitroaromatics reduction on nanoferrites is generally based on the catalysts composition. In this context, the activity depends also on various factors including surface texturing, particle size, stability, distribution of metal ions among tetrahedral (A) sites and octahedral (B) sites of the cubic spinel lattice, and the redox properties of metal ions. In particularly, our nanoferrites exhibited effective catalytic reduction of 4-NP than Ni@Au/KCC-1 nanocatalyst [55], Au/graphene [56] and Carbon@Au [57]. In ferrites, the metal ions present in the octahedral sites; that exposed on the surface, play a crucial role in catalysis since it has longer bond length. Thus, it can interact freely with the reactant molecules. Herein, when our synthesized nanoferrites are added to the reaction media; the nitrophenol/nitroaniline, the borohydride ions (produced by the ionization of NaBH_4 in aqueous medium) diffuse from the aqueous solution toward the nanoferrites surface.

Therefore, ferrites containing metal ions act as a medium to transfer electrons from BH_4^- to nitrophenol/nitroaniline and thus lead to the formation of aminophenol/phenyldiamine. On the other hand, the aqueous medium provides the H^+ ions required for the reduction of nitrocompounds. The faster the electron transfers, the higher the value of the rate constant. It is evident that the catalytic reaction was the fastest in case of MnFe_2O_4 compared to CoFe_2O_4 those exceeded that of ZnFe_2O_4 . The values of rate constants for the reduction of 4-NP, 4-NA and 2,4,6-NP on MnFe_2O_4 catalyst were the highest comparatively. Clearly, the presence of Mn and Co in the ferrites samples possesses a beneficial effect on the reduction reaction of nitroaromatics. It seems that crystallites size did not play a direct role on the catalytic activity since MnFe_2O_4 that presented the highest activity indicated the highest size that comprised of 10.6 nm (Table 1). Since the difference in average crystallites size between the lowest (6.27 nm) and the highest ferrite is approximately ~ 4 , it is expected at such low crystallites size region (6–10 nm), an increase in the fraction of low coordination metal sites is exhibited that in turn promote adsorption of the reactants [58]. The catalytic activity of MnFe_2O_4 was the highest due to the presence of both Mn^{2+} and Fe^{3+} ions in the octahedral sites of the ferrite sub-lattice. Because of this, there is an inter-valence electron charge transfer between Mn^{2+} – Mn^{3+} and Fe^{2+} – Fe^{3+} ion pairs, which enhances its catalytic activity. In case of CoFe_2O_4 , Co^{2+} – Co^{3+} and Fe^{2+} – Fe^{3+} ion pairs are also present where in ZnFe_2O_4 , only Fe^{2+} – Fe^{3+} ion pairs are present [59]. Therefore, it shows reduced catalytic activity in comparison to $\text{Mn}(\text{Co})\text{Fe}_2\text{O}_4$. The lower catalytic activity of ZnFe_2O_4 was conceivably due to its larger lattice parameter values. Due to the large size of Zn^{2+} ion, the lattice expands and the hopping length between Fe^{2+} – Fe^{3+} ions increases. This indeed delayed the inter-valence electron transfer between later ions, resulting in a decreased catalytic activity. Also, MnFe_2O_4 presented the highest hydration value (Table 2) indicating the high adsorption ability of this specific catalyst that indeed substantiated due to residual organics depicted by the TGA technique. This is important since it is acknowledged that good adsorption is an important step prior proceeding to the catalytic reaction. It is wise mentioning that residual organics did not affect much the pore volume in MnFe_2O_4 as exhibited for other ferrites comprehending the probability of acquiring the reaction not only on the surface but also inside the mesopore structure. Because it presented the highest pore volume ($0.227 \text{ cm}^3/\text{g}$) and pore radius (6.75 nm) values and thus has the ability to accept for example nitrophenol molecules of kinetic diameter $0.66 \times 0.43 \text{ nm}$. This indeed can be acquired for 4-NA and 4-NP where the facile reduction of the former is attributed to increasing the residual positive charges created on it compared to that on the later. Indeed, 2,4,6-NP owns more positive charges than other nitroaromatics but the steric hindrance is the much effective factor affecting its reduction activity.

4. Conclusion

In conclusion, MFe_2O_4 ($\text{M} = \text{Zn, Co, Mn}$) nanoparticles (6–10 nm) were successfully synthesized in a pure spinel form using a PVA template-engaged reaction via a sol gel-hydrothermal technique followed by heating at 573 K for 6 h in air. These materials exhibited high catalytic reduction capabilities toward 4-NA and 4-NP and 2,4,6-NP. The merits of the versatile nanostructures and the high magnetic properties make MnFe_2O_4 nanoparticles very prospective candidates for nitroaromatics reduction under dark conditions with great performances exceeded those in literatures under similar conditions. The significant enhancement in reduction activity can be ascribed to the MnFe_2O_4 surface that was favorable as an efficient adsorbent; in the sense of increasing mesoporosity character via enhancing pore volume and pore radius comparatively, and to

the inter-valence electron charge transfer between Mn^{2+} – Mn^{3+} and Fe^{2+} – Fe^{3+} ion pairs. Magnetic measurements through VSM indicated an increase in the highest saturation magnetization (MS) of MnFe_2O_4 that argued to an increase in the concentration of the Fe^{+3} ions in the octahedral sites. It has been shown that AO and BQ enhances markedly the catalytic reduction of nitro aromatics; compared to *tert*-butanol, when added in small amounts. More correlations of the effects of these organic additives on the nitroaromatics reduction are under investigation and promising results are on the way to be obtained.

Appendix A. Supplementary data

Supplementary data associated with this article can be found, in the online version, at <http://dx.doi.org/10.1016/j.apcatb.2015.08.005>

References

- [1] J.R. Chiou, B.H. Lai, K.C. Hsu, D.H. Chen, J. Hazard. Mater. 248–249 (2013) 394–400.
- [2] Y. Shaoqing, H. Jun, W. Jianlong, Radiat. Phys. Chem. 79 (2010) 1039–1046.
- [3] M. Megharaj, H.W. Pearson, K. Venkateswarlu, Arch. Environ. Contam. Toxicol. 21 (1991) 578–584.
- [4] R. Dai, J. Chen, J. Lin, S. Xia, S. Chen, Y. Deng, J. Hazard. Mater. 170 (2009) 141–143.
- [5] A.C. Apolinario, A.M.T. Silva, B.F. Machado, H.T. Gomes, P.P. Araujo, J.L. Figueredo, Appl. Catal. B Environ. 84 (2008) 75–86.
- [6] V. Maurino, C. Minero, E. Pelizzetti, P. Piccinini, N. Serpone, H. Hidaka, J. Photochem. Photobiol. A Chem. 109 (1997) 171–176.
- [7] P. Xiong, Y. Fu, L. Wang, X. Wang, Chem. Eng. J. 195–196 (2012) 149–157.
- [8] F.R. Zaggout, N.A. Ghalwa, J. Environ. Manag. 86 (2008) 291–296.
- [9] X. Zhu, J. Ni, Electrochim. Acta 56 (2011) 10371–10377.
- [10] Y.Y. Chu, Y. Qian, W.J. Wang, X.L. Deng, J. Hazard. Mater. 199–200 (2012) 179–185.
- [11] C. Rizhi, D. Yan, X. Weihong, X. Nanping, Chin. J. Chem. Eng. 15 (2007) 884–888.
- [12] Z. Wu, J. Chen, Q. Di, M. Zhang, Catal. Commun. 18 (2012) 55–59.
- [13] Y. Du, H. Chen, R. Chen, N. Xu, Appl. Catal. A Gen. 277 (2004) 259–264.
- [14] K.I. Min, J.S. Choi, Y.M. Chung, W.S. Ahn, R. Ryoo, P.K. Lim, Appl. Catal. A Gen. 337 (2008) 97–104.
- [15] H.V.K. Udupa, M.V. Rao, Electrochim. Acta 12 (1967) 353–361.
- [16] K. Polat, M.L. Aksu, A.T. Pekel, J. Appl. Electrochem. 32 (2002) 217–223.
- [17] F. Taghavi, C. Falamaki, A. Shabanov, L. Bayrami, R. Roumianfar, Appl. Catal. A Gen. 407 (2011) 173–180.
- [18] R. Chen, Q. Wang, Y. Du, W. Xing, N. Xu, Chem. Eng. J. 145 (2009) 371–376.
- [19] S. Gazi, R. Ananthakrishnan, Appl. Catal. B Environ. 105 (2011) 317–325.
- [20] (a) M.M. Mohamed, M.S. Al-Sharif, Appl. Catal. B Environ. 142–143 (2013) 432–441;
(b) M.M. Mohamed, M.S. Al-Sharif, Mater. Chem. Phys. 136 (2012) 528–537.
- [21] M. Kumarraja, K. Pitchumani, Appl. Catal. A Gen. 265 (2004) 135–139.
- [22] Y. Kojoma, K. Suzuki, K. Fukumoto, M. Sasaki, T. Yamamoto, Y. Kawai, Int. J. Hydrogen Energy 27 (2002) 1029–1034.
- [23] U.B. Demirci, F. Garin, J. Mol. Catal. A Chem. 279 (2008) 57–62.
- [24] R.R. Mandlimath, B. Gopal, J. Mol. Catal. A Chem. 350 (2011) 9–15.
- [25] Y.C. Chang, D.H. Chen, J. Hazard. Mater. 165 (2009) 664–669.
- [26] X. Du, J. He, J. Zhu, L. Sun, S. An, Appl. Surf. Sci. 258 (2012) 2717–2723.
- [27] R.J. Kalbasi, A.A. Nourbakhsh, F. Babaknezhad, Catal. Commun. 12 (2011) 955–960.
- [28] J. Feng, L. Sua, Y. Ma, C. Ren, Q. Guo, X. Chen, Chem. Eng. J. 221 (2013) 16–24.
- [29] S. Singhal, T. Namgyal, J. Singh, K. Chandra, S. Bansal, Ceram. Int. 37 (2011) 1833–1837.
- [30] I.D. Smiciklas, S.K. Milonje, P. Pfendt, S. Raicevic, Sep. Purif. Technol. 18 (2000) 185–194.
- [31] H.E. Kissinger, J. Res. Natl. Bur. Stand. 57 (1956) 217–221.
- [32] A.K. Burnham, R.L. Braun, Energy Fuels 13 (1999) 1–22.
- [33] A.W. Coats, J.P. Redfern, Nature 201 (1964) 68–69.
- [34] H.H. Horowitz, G. Metzger, Anal. Chem. 35 (1963) 1464–1468.
- [35] M. Nath, P. Arora, Synth. React. Inorg. Met. Org. Chem. 23 (1993) 1523–1546.
- [36] A.A. Soliman, S.M. El-Medani, O.A.M. Ali, J. Therm. Anal. Calorim. 83 (2006) 385–392.
- [37] J.Z. Jiang, P. Wynn, S. Morup, T. Okada, F.J. Berry, Nanostruct. Mater. 12 (5) (1999) 737–740.
- [38] S.U. Nandanwar, M. Chakraborty, Chin. J. Catal. 33 (2012) 1532–1541.
- [39] S.M. Su, C. Hea, V.K. Sharma, M.A. Asia, D. Xia, X.-Z. Li, H. Deng, Y. Xiong, J. Hazard. Mater. 211–212 (2012) 95–103.
- [40] R. Tholkappian, K. Vishista, Physica B 448 (2014) 177–183.
- [41] F. Li, H. Wang, L. Wang, J. Wang, J. Magn. Magn. Mater. 309 (2007) 295–299.
- [42] R. Kalai Selvan, C.O. Augustin, C. Sanjeeviraja, V.G. Pol, A. Gedanken, Mater. Chem. Phys. 99 (2006) 109–116.
- [43] K. Laohasurayotin, S. Pookboonmee, D. Viboonratanasri, W. Kangwansupamonkon, Mater. Res. Bull. 47 (2012) 1500–1507.
- [44] L. Zhen, K. He, C.Y. Xu, W.Z. Shao, J. Magn. Magn. Mater. 320 (2008) 2672–2675.
- [45] J. Wang, Q.W. Chen, C. Zeng, B.Y. Hou, Adv. Mater. 16 (2004) 137.
- [46] S.Y. Lian, E.B. Wang, L. Gao, Z.H. Kang, D. Wu, Y. Lan, L. Xu, Solid State Commun. 132 (2004) 375.
- [47] K. He, C.Y. Xu, L. Zhen, W.Z. Shao, Mater. Lett. 61 (2007) 3159.
- [48] A. Manikandan, J. Judith Vijaya, M. Sundararajan, C. Meganathan, L. John Kennedy, M. Bououdina, Superlattices Microstruct. 64 (2013) 118–131.
- [49] M.M. Mohamed, Microporous Mesoporous Mater. 109 (1–3) (2008) 445.
- [50] Q. Cui, B. Xia, St. Mitzscherling, A. Masic, L. Li, M. Bargheer, H. Möhwald, Colloids Surf. A Physicochem. Eng. Aspects 465 (2015) 20–25.
- [51] A. Goyal, S. Bansal, P. Samuel, V. Kumar, S. Singhal, J. Mater. Chem. A 2 (2014) 18848–18860.
- [52] Z.M. El-Bahy, Appl. Catal. A Gen. 468 (2013) 175–183.
- [53] M.M. Ibrahim, S.A. Ahmed, K.S. Khairou, M.M. Mohamed, Appl. Catal. A Gen. 475 (2014) 90–97.
- [54] J.T. Nurmi, P.G. Tratnyek, Environ. Sci. Technol. 36 (2002) 617–624.
- [55] Y. Fu, H. Chen, X. Sun, X. Wang, Appl. Catal. B Environ. 111–112 (2012) 280–287.
- [56] X. Le, Z. Dong, W. Zhang, X. Li, J. Ma, J. Mol. Catal. A Chem. 395 (2014) 58–65.
- [57] J. Li, C.Y. Liu, Y. Liu, J. Mater. Chem. 22 (2012) 8426–8430.
- [58] P. Zhang, C.L. Shao, X.H. Li, M.Y. Zhang, X. Zhang, C.Y. Su, N. Lu, K.X. Wang, Y.C. Liu, Phys. Chem. Chem. Phys. 15 (2013) 10453–10458.
- [59] T.M. Clark, B.J. Evans, IEEE Trans. Magn. 33 (1997) 3745–3747.